

## Microscopic insights into poly- and mono-crystalline methane hydrate dissociation in Na-montmorillonite pores at static and dynamic fluid conditions

Fang, Bin; Lü, Tao; Li, Wei; Moulton, Othonas A.; Vlugt, Thijs J.H.; Ning, Fulong

**DOI**

[10.1016/j.energy.2023.129755](https://doi.org/10.1016/j.energy.2023.129755)

**Publication date**

2024

**Document Version**

Final published version

**Published in**

Energy

**Citation (APA)**

Fang, B., Lü, T., Li, W., Moulton, O. A., Vlugt, T. J. H., & Ning, F. (2024). Microscopic insights into poly- and mono-crystalline methane hydrate dissociation in Na-montmorillonite pores at static and dynamic fluid conditions. *Energy*, 288, Article 129755. <https://doi.org/10.1016/j.energy.2023.129755>

**Important note**

To cite this publication, please use the final published version (if applicable).  
Please check the document version above.

**Copyright**

Other than for strictly personal use, it is not permitted to download, forward or distribute the text or part of it, without the consent of the author(s) and/or copyright holder(s), unless the work is under an open content license such as Creative Commons.

**Takedown policy**

Please contact us and provide details if you believe this document breaches copyrights.  
We will remove access to the work immediately and investigate your claim.

***Green Open Access added to TU Delft Institutional Repository***

***'You share, we take care!' - Taverne project***

**<https://www.openaccess.nl/en/you-share-we-take-care>**

Otherwise as indicated in the copyright section: the publisher is the copyright holder of this work and the author uses the Dutch legislation to make this work public.



# Microscopic insights into poly- and mono-crystalline methane hydrate dissociation in Na-montmorillonite pores at static and dynamic fluid conditions

Bin Fang<sup>a</sup>, Tao Lü<sup>b,c</sup>, Wei Li<sup>d</sup>, Othonas A. Moutos<sup>e</sup>, Thijs J.H. Vlugt<sup>e</sup>, Fulong Ning<sup>d,f,\*</sup>

<sup>a</sup> School of Mathematics and Physics, China University of Geosciences, Wuhan, 430074, China

<sup>b</sup> School of Automation, China University of Geosciences, Wuhan, 430074, China

<sup>c</sup> Hubei Key Laboratory of Advanced Control and Intelligent Automation for Complex Systems, Wuhan, 430074, China

<sup>d</sup> Faculty of Engineering, China University of Geosciences, Wuhan, Hubei, 430074, China

<sup>e</sup> Engineering Thermodynamics, Process & Energy Department, Faculty of Mechanical Engineering, Delft University of Technology, Leeghwaterstraat 39, Delft, 2628CB, the Netherlands

<sup>f</sup> National Center for International Research on Deep Earth Drilling and Resource Development, China University of Geosciences, Wuhan, 430074, China

## ARTICLE INFO

Handling Editor: Wojciech Stanek

### Keywords:

Poly- and mono-crystalline hydrates  
Molecular simulation  
Dissociation behaviors  
Na-montmorillonite pore  
Static and dynamic fluid conditions

## ABSTRACT

Knowledge on the kinetics of gas hydrate dissociation in clay pores at static and dynamic fluid conditions is a fundamental scientific issue for improving gas production efficiency from hydrate deposits using thermal stimulation and depressurization respectively. Here, molecular dynamics simulations were used to investigate poly- and mono-crystalline methane hydrates in Na-montmorillonite clay nanopores. Simulation results show that hydrate dissociation is highly sensitive to temperature and pressure gradients, but their effects differ. Temperature changes increase thermal instability of water and gas molecules, leading to layer-by-layer dissociation from the outer surface. Under flow conditions, laminar flow predominates in nano-pores, and non-Darcy flow occurs due to clay-fluid interactions. Viscous flow disrupts hydrogen bonding at the hydrate surface, enhancing kinetic instability of water. Grain boundaries of polycrystalline hydrates are less stable compared to bulk phases and preferentially decompose, forming new dissociation fronts. This accelerates dissociation compared to mono-crystalline hydrates. Fracture occurs at the grain boundaries of polycrystalline hydrate in the fluid, resulting in separate hydrate crystal grains. This fracture process further accelerates hydrate dissociation. In flow systems, methane nanobubbles form in fluid and readily transport with fluid flow. Unlike surface nanobubbles at static conditions, these liquid nanobubbles exhibit mobility. The findings of this study can contribute to a better understanding of the complex phase transition behavior of hydrate in confined environment, and provide theoretical support for improving production control technology.

## 1. Introduction

The urgent need to address the energy crisis has arisen from the rapid increase in global consumption of conventional fossil fuels and geopolitical instability. Unconventional energy resources like natural gas hydrates (NGH) have gained attention due to their abundance and potential as a natural gas source. NGHs offer a viable solution to the ever-increasing global energy demand [1–3]. NGHs, hosting primarily methane as guest molecules, are non-stoichiometric, ice-like crystalline compounds where the polyhedral cages formed by the concurrent hydrogen bonding (H-bond) framework of concomitant water molecules

which accommodate these guest molecules [4]. Three main types of NGH crystal structures, including cubic sI and sII, as well as hexagonal sH, are identified, with their formation contingent upon the guest molecules' nature [4]. NGHs are typically occurring in marine sediments, making up over 90 % of NGH reserves, as well as in permafrost regions [5,6]. The estimated reserves of NGHs are twice that of the reserves of all other fossil fuels combined [7]. Therefore, the development of NGHs, specifically in marine sediment deposits, has received extensive attention from governments globally [8]. Additionally, hydrates have significant potential for various industrial applications related to water, energy, and the environment, such as CO<sub>2</sub> capture and sequestration (CCS) [9], flow assurance [10], hydrogen storage [11], seawater

\* Corresponding author. Faculty of Engineering, China University of Geosciences, Wuhan, Hubei 430074, China.

E-mail address: [nflzx@cug.edu.cn](mailto:nflzx@cug.edu.cn) (F. Ning).

<https://doi.org/10.1016/j.energy.2023.129755>

Received 21 August 2023; Received in revised form 21 November 2023; Accepted 22 November 2023

Available online 27 November 2023

0360-5442/© 2023 Elsevier Ltd. All rights reserved.

Nomenclature		$5^{12}6^2$	cages constructed by twelve pentagons and two hexagons
$f_{ex}$	external force, kJ/(mol·Å)	<i>Subscript</i>	
$p$	pressure, MPa/nm	$F_3$	order parameter
$T$	temperature, K	$F_4$	four-body parameter
$L_x$	the box size in the x direction, Å	<i>Acronyms</i>	
$L_y$	the box size in the y direction, Å	NGH	natural gas hydrate
$W$	the width of clay pore, Å	H-bond	hydrogen bond
$i, j, k$	water oxygen number	MD	molecular dynamics
$v$	hydrate dissociation rate	EF-NEMD	external field non-equilibrium molecular dynamics
$t$	time	GB	grain boundary
$N_t$	the number of hydrate cages at time $t$	PHS	poly-crystalline hydrate system
$N_0$	the initial number of hydrate cages	MHS	mono-crystalline hydrate
<i>Greek</i>		PBC	periodic boundary condition
$\theta$	angle formed by adjacent water oxygen	SCS	South China Sea
$\varphi$	H–O···O–H torsion angle	$NpT$	statistical ensemble with a constant particle number $N$ , pressure $p$ and temperature $T$
<i>Superscript</i>		$NVT$	statistical ensemble with a constant particle number $N$ , volume $V$ and temperature $T$
$5^{12}$	cages cages constructed by twelve pentagons		

desalination [12], waste water treatment [13], and gas transport [14], all of which involve phase changes of hydrates.

Marine hydrate resources are primarily located within micro- or nano-scale porous sediments consisting of sand and clay minerals, with varying degrees of contact with solid particle surfaces [2]. The permeability of these hydrate reservoirs is typically low [2]. Thermal stimulation and depressurization have been proposed as effective methods for extracting natural gas from hydrate resources [15]. During the extraction process, by altering the local temperature and pressure conditions of NGH reservoirs, hydrates dissociate into the desired natural gas and liquid water within the sediment. However, the complexity of sedimentary environments, combined with the characteristics of volatile oil reservoirs, contributes to the increased complexity of phase changes in NGHs and the flow of water and gas during hydrate exploration and

development. These factors can potentially pose a higher risk of methane leakage, making the commercial extraction of NGH resources a significant challenge. The exploitation of hydrates requires a multidisciplinary approach, incorporating knowledge from geological engineering, engineering thermophysics, and chemical engineering, spanning multiple length- and time-scales from micro to macro. The foundation is to understand the kinetic processes and the main controlling factors of marine hydrate dissociation for a wide range of gas production conditions, especially within confined pores. The general overview of the problem under study is shown in Fig. 1.

In the mid-1980s, Kim et al. [16] based on in-situ dissociation experiments derived an equation describing gas hydrate dissociation kinetics. This study suggested that the dissociation rate of gas hydrates in liquid phase is proportional to the hydrate phase surface area and the

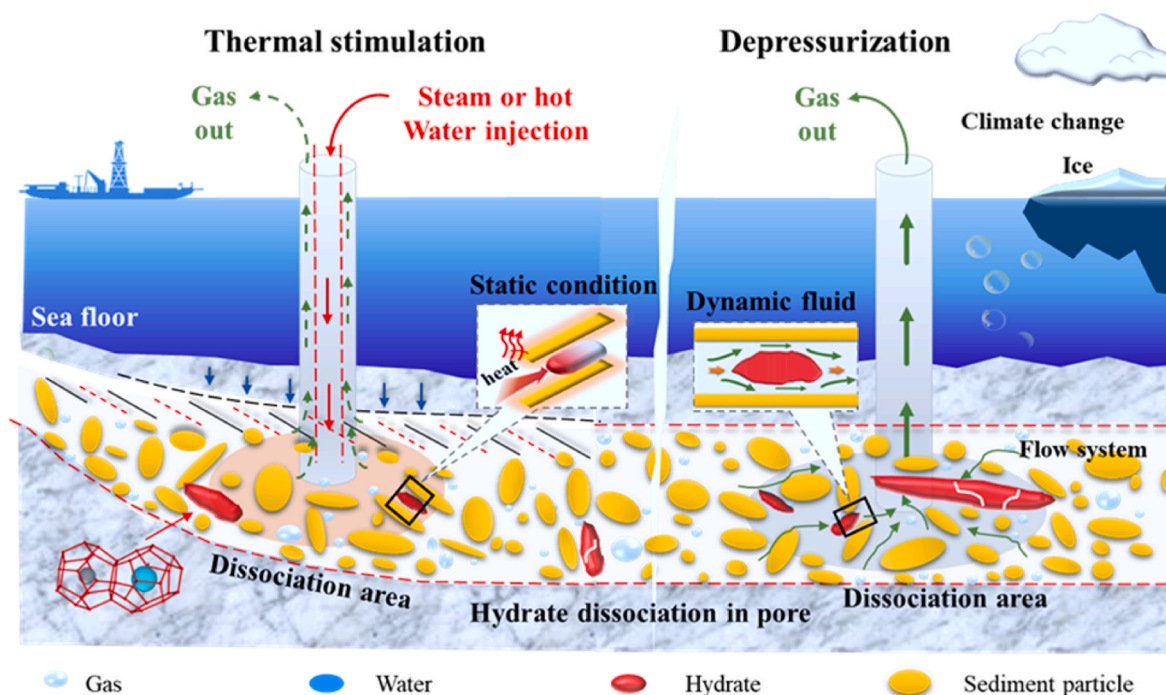


Fig. 1. Schematic diagram of hydrate dissociation in marine sediments under thermal stimulation and depressurization process.

fugacity difference of methane at the equilibrium pressure and the dissociation pressure. Jamaluddin [17], Goel [18], and others subsequently revised the equation by Kim et al. [16] For the more complex low-permeability sedimentary environment of ocean reservoirs, researchers have attempted to reveal the dissociation behavior and its control mechanism at the pore scale. Pore environment can shift the condensation curve of methane [19], and alter the transport pathways of guest and host molecules, ultimately controlling the behavior of hydrate formation, growth, and dissociation phase transition [20–26]. Experimental results have shown that the gas hydrate dissociation rate is influenced by factors such as the properties of the hydrate sediment [27, 28], heat transfer rate [28], hydrate saturation [29], and fluid-solid migration [30]. These factors affect the occurrence of hydrates in reservoir pores and are closely related to the efficiency of hydrate dissociation and mass transfer behavior during the exploitation process after dissociation. Although micro-detection techniques such as X-ray CT and NMR can be used to observe the phase transition process of gas hydrates in sediments [29,31–36], the intricate and diverse characteristics of pore structures and surface physicochemical properties pose challenges in accurately understanding the patterns of phase transition behavior in low-porosity and low-permeability reservoirs.

Molecular dynamics (MD) simulation, as a relatively new research tool, can intuitively present the separation process of natural gas and water in hydrate by simulating snapshots at the molecular level [24, 37–43], and explain the necessity of the hydrate dissociation pathway from an energy perspective by energy barrier calculation [39]. The surface of hydrate clusters in dissociation induced by high temperature exhibits a series of rapid decay processes and forms transition states, which are characterized by a progressive and random layer-by-layer stripping from the outside to the inside at a static condition [24, 37–41]. MD studies have been conducted to explore the kinetic process of liquid-phase hydrate dissociation due to the influence of various factors, such as temperature [44,45], pressure [40], salt [46], presence of bubbles [47], and external electric fields [48]. Various hydrate dissociation kinetic models have been developed, such as the Gibbs-Thomson equation-based dissociation model [49] and the Chen-Guo equation-based dissociation model [50].

Most of MD studies focuses on the hydrate dissociation process in open-water environments, in recent years, there has been growing attention to the study of hydrate dissociation within sediment-confined spaces by heating. Bagherzadeh [24], Liao [25] and Fang [23,26] have studied the hydrate dissociation behavior in single nanopores of quartz sand and microcracks of clay minerals by constructing a two-dimensional “sandwich” pore model (which can be divided into three layers of solid phase - hydrate phase - solid phase). The simulation results show that the dissociation process of the hydrate phase is similar to that in the liquid phase. To achieve separation of methane hydrate, it is necessary to first break or partially break the spatial lattice structure formed by the host molecular constituents, and the hydrate grains undergo phase transition dissociation in a “shrinking core” manner [23–26]. The hydrate dissociation rate is significantly affected by the interface [24], which is consistent with the experimental results [51]. MD simulations result also indicate that the invasion of drilling fluid plays a significant role in the dissociation of hydrates by affecting the fluid-hydrate interactions [25]. In the above simulations, hydrate dissociation is induced under static conditions through heating, phase transition process in the fluid flow environment induced by depressurization during exploitation have been few discussed.

Prior research on the dissociation of gas hydrates using MD simulation has primarily emphasized on monocrystalline hydrates, disregarding the fact that gas hydrates occur as polycrystals in both natural settings and laboratory environments [52,53]. Polycrystalline hydrates are composed of a network of interconnected crystals, known as grains, with distinct orientations and boundaries between them. The structure at grain boundaries differs from the bulk crystal lattice, characterized by the presence of nonstandard crystal cages and small gas clusters [54,55].

Compared to monocrystalline hydrates, the presence of grain boundaries in polycrystalline hydrates can lead to differences in their mechanical stability [54] under mechanical loading and thermal stability [55].

Benefiting from MD simulation, the microscale dissociation processes of mono-crystal hydrates within pores under heating conditions is being revealed gradually. However, some questions remain unclear, including the role of grain boundaries in polycrystalline hydrate dissociation within pores; Additionally, depressurization is more efficient for the process of trial mining of hydrate resources [56–58], the behavior of hydrate dissociation in flow system during depressurization-based gas extraction still unclear. Here, we constructed multiphase hydrate dissociation configurations containing both mono- and polycrystalline hydrates to study the impact of grain boundaries on hydrate dissociation in nanopores. External field non-equilibrium MD (EF-NEMD) simulations are introduced to create a flow system in pore and explore the dissociation behavior of hydrates at dynamic conditions, addressing the limitations of previous classical MD simulation studies.

This study represents fundamental research aimed at the safe and efficient exploitation of hydrates, which may have significant implications for alleviating energy shortages, achieving carbon neutrality, and fostering sustainable development. The remaining structure of this study is as follows: First, the method is described in Section 2, including the initial configurations, force fields, detail of MD and EF-NEMD simulation configuration. In Section 3, the equilibrium structures of ploy- and mono-crystalline hydrate within clay pore are discussed. Based on the structure, we study the hydrate dissociation process by heating at static conditions. Subsequently, hydrate dissociation behavior and nanobubble formation in a flow system induced by pressure gradient are studied. Finally, Section 4 presents a summary of the study's conclusions.

## 2. Method

### 2.1. Initial configuration

Two multiphase initial systems are constructed with both initial configurations consisting of clay minerals, a methane hydrate phase, and two liquid water phases (Fig. 2). The clay pore is constructed by two Na-montmorillonite slabs and a methane hydrate phase located in the pore phase with two water phases in both sides. For the Na-montmorillonite solid phase, the unit cell is created based on the 2:1 structure of pyrophyllite which is comprised of one sandwiched Al–O octahedral layer and two Si–O opposing tetrahedral layers, The lattice parameters of the pyrophyllite unite cell are from the American Mineralogist Crystal Structure Database [59]. The final structure of montmorillonite is constructed by random isomorphic substitution of  $Al^{3+}$  by  $Mg^{2+}$  atoms in the octahedral layer and  $Si^{4+}$  by  $Al^{3+}$  atoms in the tetrahedral layer, respectively [60]. The Loewenstein's rule [61] should be obeyed in isomorphic substitutions for avoiding two substitutions in adjacent atoms. The isomorphic substitutions lead to a negative charge of montmorillonite and was compensated by interlayer sodium cations ( $Na^+$ ), that are randomly put in the water phase in the nanopore. The chemical formula for the unit clay is  $Na_{0.75}(Si_{7.75}Al_{0.25})(Al_{3.5}Mg_{0.5})O_{20}(OH)_4$  and each solid slab is constructed by  $20 \times 1 \times 7$  unit cells.

The construction of the unit cell in methane hydrate is identical to that in Takeuchi's work [62]. The water oxygen coordinates are determined by X-ray crystallography results, while the positions of water hydrogen atoms are adjusted according to the Bernal-Fowler rule to minimize both dipole moment and potential energy of the system. The methane molecules fully occupy the hydrate cages formed by hydrogen-bonded water molecules. The unit cell of methane hydrate adopts an *sf* structure with a lattice parameter of 12.03 Å [62]. The polycrystalline hydrate phase is constructed by two monocrystalline hydrate grains, one is a  $5 \times 5 \times 3$  supercell, the other supercell is also constructed by  $5 \times 5 \times 3$  unit cell which was rotated by 90° along the Y-axis. The grain boundary (GB) shown in Fig. 2(a) joins the (100) and

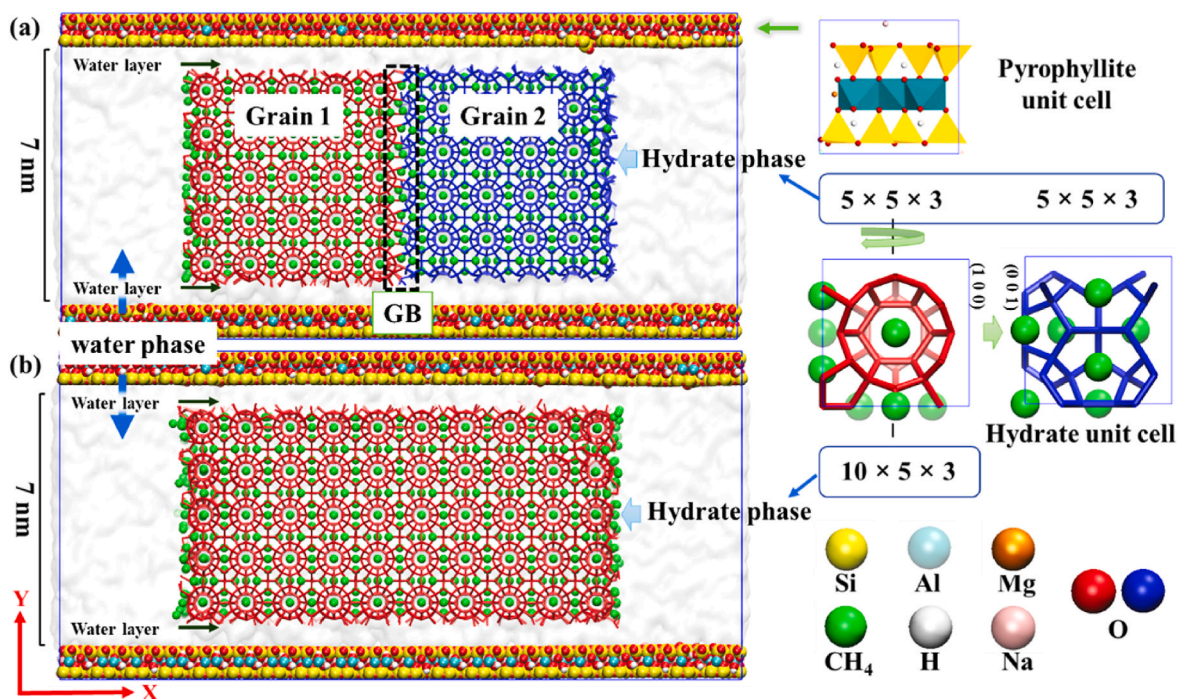


Fig. 2. Initial multi-phases simulation configurations with (a) polycrystalline and (b) monocrystalline hydrate phases in the clay interlayer. The Na-montmorillonite clay phase, liquid water phase, hydrate phase, and water layer between hydrate and clay surface are shown. The unit cells of hydrate and clay are shown. Two monocrystalline hydrate grains in the PHS are colored by red and blue respectively. Atom color scheme: Si, yellow; Al, cyan; Mg, orange; C, green; H, white; Na, pink; O, red and blue.

(001) crystalline planes of the two monocrystalline methane hydrates in the x-direction. The monocrystalline hydrate is built by the  $10 \times 5 \times 3$  supercell and shown in Fig. 2(b).

In the pore space, hydrate phases are located in the central region, while the remaining space on both sides of the hydrate phase is occupied by liquid water molecules within the clay pores. It is important to note that a thin layer of water exists between the clay and hydrate surfaces. This arises from the incomplete translation of water molecules near the solid surface into the hydrate phase, as observed in experiments and simulations [63–66]. This interlayer plays a role in accommodating the mismatch between clay and hydrate crystals [63–66]. There are 11200 atoms in the two clay slabs, 7879 water molecules in water phase, along with 210  $\text{Na}^+$  ions, 6900 water molecules and 1110 methane molecules in the hydrate phase in each initial simulation configuration. In this work, the initial systems consisting of poly-crystalline hydrate phase or mono-crystalline hydrate phase are referred to as PHS and MHS, respectively.

## 2.2. Force fields and simulation details

The TIP4P/ice [67], OPLS-UA [68], and CLAYFF [69] force fields are used to model water, methane, and Na-montmorillonite substrates (including  $\text{Na}^+$  ions), respectively. The parameters for these force fields are listed in Table S1 of the Supporting Information. The TIP4P/ice water model is an adequate choice for predicting the coexistence equilibrium temperatures and pressures of the hydrate (or ice) by classical MD simulations [67,70]. The CLAYFF force field is suitable for simulating the phase change process of hydrates in clay systems [25,71,72], as well as interfacial phenomena with aqueous solutions [73]. Newton's equations of motion are integrated using the leapfrog algorithm [74] with a time step of 1 fs. The Lennard-Jones potential is used to describe the van der Waals interactions [75], and the Lorentz-Berthelot combining rules are used for the dissimilar atom pairs [76]. The short-range nonbonded interactions (including the van der Waals and Coulomb interactions) are calculated with a cutoff distance of 1.2 nm.

Long-range electrostatic interactions are handled by the Particle-Mesh Ewald summation method [77]. Periodic boundary conditions (PBCs) are used in all directions, and all the simulations are performed by the Gromacs software (version 2018.2) [78,79]. The identification of polyhedral cages, including the  $5^{12}$  and  $5^{12}6^2$  cages, is accomplished using a cage identification code developed by Jacobson et al. [80].

## 2.3. Equilibrium molecular dynamics simulations

In each MD simulation, the energy of the systems is minimized for the two initial configurations using a conjugate gradient algorithm [81]. A 2 ns  $NpT$  simulation is performed to relax the temperature and pressure of each system. The equilibrium pressure and temperature are set to 14.5 MPa and 287 K, respectively, which is approximately equal to the average pressure and temperature of the South China Sea (SCS) hydrate reservoir [82]. The velocity rescaling method incorporating a stochastic term is used to couple the temperature with a thermostat constant of 0.1 ps, and the pressure is controlled using the Parrinello-Rahman extended-ensemble pressure coupling method with a barostat constant of 1.0 ps [83,84]. The equilibrated system was used for the production of MD simulations. A long 10 ns NVT ensemble simulations was performed for each simulation. These production MD simulations are used to study the temperature effects on hydrate dissociation dynamic behavior with temperature settings to 287, 307, 327, 337, and 347 K, respectively. Setting a high dissociation temperature is advantageous for analyzing the hydrate dissociation behavior in the pore within the constraints of limited simulation time.

## 2.4. External field nonequilibrium molecular simulations

To investigate the impact of depressurization-induced pressure gradient on gas production, we use external field non-equilibrium MD molecular dynamics simulations to replicate the hydrate dissociation process in a multi-phase flow system. We apply a high-pressure gradient ranging from 0 to 50 MPa/nm. Despite the deviation from the actual

pressure gradient setting, this high-pressure gradient is necessary because the directional flow of water and gas molecules within the nanopore, driven by the pressure gradient, cannot be adequately facilitated by a small external force alone. Thermal fluctuations and surface interactions can counterbalance this external force. The use of a high-pressure gradient helps to optimize computational efficiency and has been widely utilized in previous studies focused on simulating nanoscale flow [85,86]. In the flow direction ( $x$ ), the external force acting on each atom can be obtained by Ref. [85]:

$$f_{\text{ex}} = -\frac{dp}{dx} \frac{L_x L_z W}{N} \times 6.022 \times 10^{-5} \quad (1)$$

where  $f_{\text{ex}}$  is the external force in the unit of  $\text{kJ}/(\text{mol} \cdot \text{\AA})$ ;  $\frac{dp}{dx}$  is the pressure gradient in the unit of  $\text{MPa}/\text{nm}$ , in our simulations,  $\frac{dp}{dx}$  is set to 0, 10, 20, 30, 40, 50  $\text{MPa}/\text{nm}$ , respectively;  $L_x$  and  $L_z$  are the box size in the  $x$  and  $z$  direction respectively,  $W$  is the width of clay pore, the unit of box size and pore size is  $\text{\AA}$ . A 10 ns NVT simulation is performed followed the equilibrium simulation for the two systems at different temperatures and pressure gradients in the  $x$  direction. Both clay sheets are kept as rigid structures.

### 3. Results and discussion

#### 3.1. Poly- and mono-crystalline hydrate structure within clay pore

The variation of the potential energy of the system and the clathrate cage number in the hydrate as a function of time is shown in Fig. S1 and Fig. S2 of the Supporting Information respectively. These figures are obtained after a 2ns  $NpT$  ensemble simulation, where the hydrate phases in the two systems reached equilibrium at 287 K and 14.5 MPa. Fig. 3 shows the water and methane density profiles along the X and Y directions for the two systems after 2 ns, respectively. In Fig. 3(a), the water density in the liquid phase is observed to be higher than that in the hydrate phase. The hydrate phases are situated between the two liquid water phases in the  $x$ -direction, indicating that partial hydrates near the liquid water phase undergo dissociation. Several methane molecules are present in the liquid phase, suggesting the release of methane from the hydrate cages and its diffusion into the surrounding liquid water layer. In the  $y$  direction (Fig. 3(b)), two water shells are visible on the solid phase, at a significantly higher water density compared to the bulk phase. This phenomenon may be attributed to adsorption effects between water and the hydrophilic solid surfaces. Similar water layers can be observed on other hydrophilic solid surfaces [23,85,86]. Several methane molecules are found within this water layer, indicating the dissociation of hydrate phases in contact with the solid phase.

The dissociation process of both polycrystalline and monocrystalline hydrate in clay pore are studied. The snapshots for both systems after 2

ns equilibrium simulation are shown in Fig. 4. To better understand the multi-phase system in clay pore, the  $F_3$  order parameter proposed by Baez and Clancy [37] and the  $F_4$  [87] order parameter are used to characterize the water molecules. The  $F_3$  order parameter can be provide a deviation of the tetrahedral structure formed by four adjacent neighbor water oxygen atoms of the target water from the standard tetrahedral structures:

$$F_{3,i} = \langle [\cos \theta_{jik} |\cos \theta_{jik}| + \cos^2 109.47]^2 \rangle_{j,k} \quad (2)$$

$$= \begin{cases} \sim 0.1 & \text{liquid water} \\ \sim 0.0 & \text{solid water (ice, hydrate)} \end{cases}$$

where  $\theta_{jik}$  is the angle formed by the center oxygen atom  $i$  and two neighbor water oxygen atoms  $j$  and  $k$  within a first spherical shell of center atom  $i$  (the radius is 3.5  $\text{\AA}$  corresponding to the distance of first minimum in the RDF of water oxygen in a liquid phase).

The  $F_4$  four-body parameter [87] is computed by the H-O ... O-H torsion angle ( $\varphi$ ). Each atom O belongs to the adjacent water molecules respectively; the H are the outer most hydrogen atoms in each adjacent water molecules:

$$F_{4,\varphi} = \langle \cos 3\varphi_i \rangle \quad (3)$$

$$= \begin{cases} \sim -0.4 & \text{ice} \\ \sim -0.04 & \text{water phase} \\ \sim 0.89 & \text{sI hydrate} \\ \sim 0.96 & \text{sII hydrate} \end{cases}$$

The  $F_3$  and  $F_4$  order parameters along the  $x$  direction at 2 ns are presented in Fig. 4. The variation of the  $F_3$  and  $F_4$  order parameter is almost the same. We used PBCs in our simulations, thus, both systems are symmetric. In the PHS system, the pore space can be divided into seven areas along the pore direction. The first area is the liquid water phase, followed by the water-hydrate interface. During the equilibrium MD simulation, the corners of the hydrate cluster, characterized by a small curvature, transition into the liquid phase. This transition is accompanied by the release of methane molecules from the hydrate cages, which diffuse into the liquid water phase. This phenomenon is induced by the Gibbs-Thomson effect [88]. As a result, the hydrate phase changes from a cubic shape to a roughly circular cross-section, a characteristic observed in both systems. Adjacent to the hydrate phase, between the two hydrate grains in the PHS system a grain boundary region exists. The  $F_3$  and  $F_4$  order parameters, as visualized in Fig. 4, effectively illustrate the changes in water molecules within different regions of the pore space. Specifically, these regions include the liquid water phase, the water-hydrate interface, and, in the case of the PHS system, a grain boundary region. The calculated order parameters reveal that water molecules in this grain boundary area are in a transitional state, which is supported by research conducted by Zhang et al. [55]. When comparing the MHS system to the PHS system, the variations in the behavior of

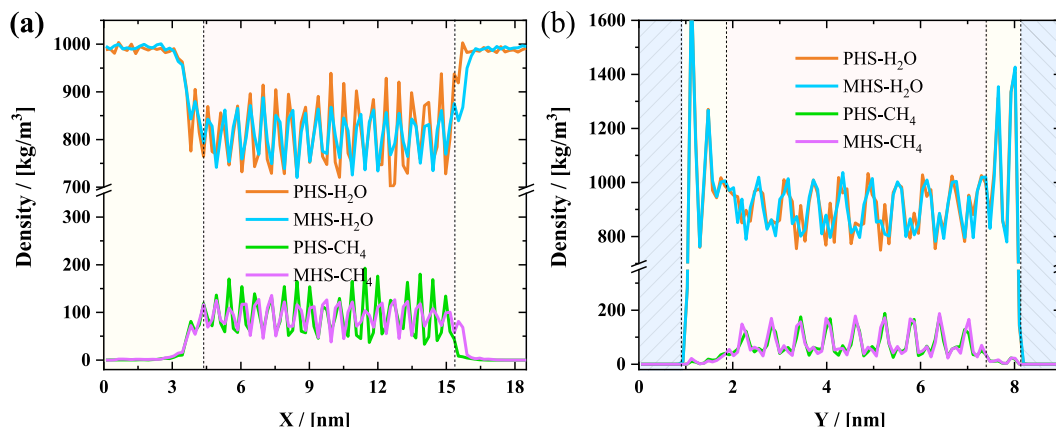


Fig. 3. Density profiles for water and methane along the (a)  $x$  and (b)  $y$  direction for the PHS and MHS systems.

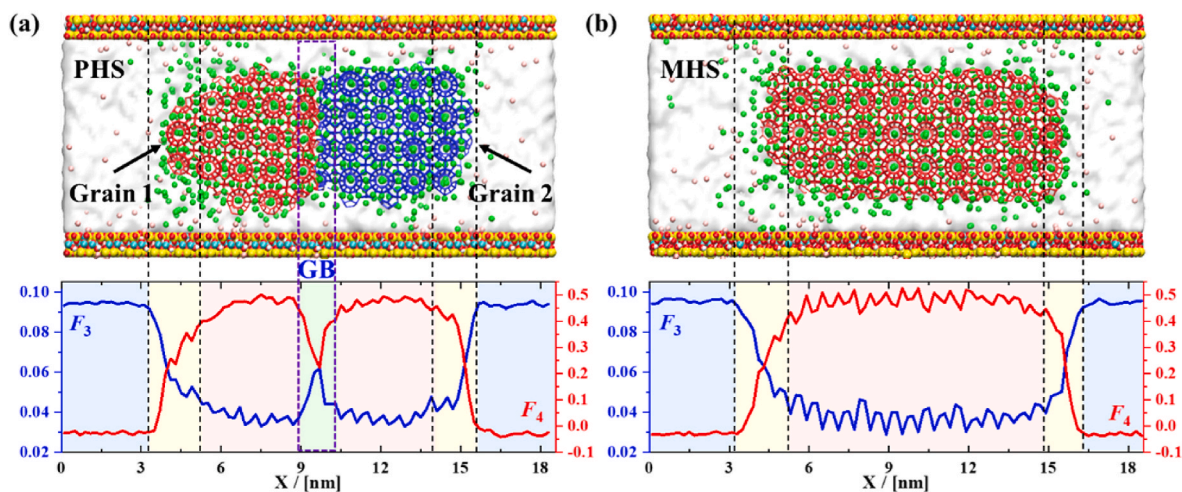


Fig. 4. Snapshots of (a) PHS and (b) MHS systems after 2 ns equilibrium MD simulation,  $F_3$  and  $F_4$  order parameters for the water molecules along the  $x$  axis are shown.

water molecules are similar in most areas, with the exception of the absence of a grain boundary region in the former.

### 3.2. Effect of temperature on hydrate dissociation

The time variation of the number of clathrate cages  $5^{12}$  and  $5^{12}6^2$  between two clay slabs for the two systems in 10.0 ns is shown in Fig. 5. In each system, the number of  $5^{12}$  cages is lower than the number of  $5^{12}6^2$  cage. This is because the ratio of the two cages is 1:3 in the unit cell of sI methane hydrate, while the trend of the changes in the quantities of these two types of crystal lattices is consistent in each simulation. At 287 K, there is minimal hydrate dissociation within the clay pore, with only slight fluctuations in the cage numbers. As the temperature increases to 307 K, 327 K, and 347 K, the hydrate phase becomes increasingly unstable, leading to a significant reduction in the number of cages over time. In the PHS system, the hydrate dissociation percentages at these temperatures are 2.5 %, 32.9 %, and 63.75 %, while in the MHS system, they are 2.0 %, 33.3 %, and 51.8 %. When the temperature reaches 347 K, complete dissociation of the hydrate phase occurs within the 10 ns simulation time, with dissociation times of 6.0 ns for the PHS system and 8.9 ns for the MHS system. These simulation results highlight the significant positive effect of temperature on hydrate dissociation, which has also been discussed in previous studies [24,37–41].

As the temperature increases, the kinetic energy of molecules in the simulated system also increases. The mean square displacements (MSD) of water and gas molecules at different temperatures are shown in Fig. 6. As expected, higher temperatures lead to larger MSD amplitudes for

water molecules. In hydrates, rising temperatures make it more likely for water molecules to break free from the constraints of the solid-phase hydrogen bonding network, thus facilitating hydrate dissociation. By applying the Einstein relationship, the self-diffusion coefficients of water and methane were calculated (Fig. 7(a)). These coefficients increase with temperature, reflecting the enhanced thermal motion. Notably, water molecules in the PHS system exhibit higher diffusion coefficients compared to the MHS system, especially at elevated temperatures. This difference is correlated with the rate of hydrate dissociation, where a faster rate allows more water molecules to escape the H-bonded framework.

Fig. 7(b) shows the average dissociation rate (computed as  $v = \langle -dN/dt \rangle$ , where  $v$  represents the dissociation rate,  $t$  is the hydrate dissociation time,  $N$  is the total hydrate cage count, and  $\langle \dots \rangle$  indicates an ensemble average). At lower temperatures (below 327 K), both the PHS and MHS systems exhibit similarly low hydrate dissociation rates, indicating minimal dissociation. However, at higher temperatures, the polycrystalline hydrate in the PHS system dissociates more rapidly than the monocrystalline hydrate in the MHS system. This difference becomes more pronounced with increasing temperature. The dissimilarity in dissociation behavior between mono-crystal and polycrystalline hydrates is particularly evident at high temperatures, in alignment with the diffusion coefficients of water and methane molecules (Fig. 7(a)). To comprehend the factors underlying this distinction, it is crucial to examine the dissociation processes of these two types of hydrate crystals.

Figs. 8 and 9 show snapshots of the hydrate dissociation process for

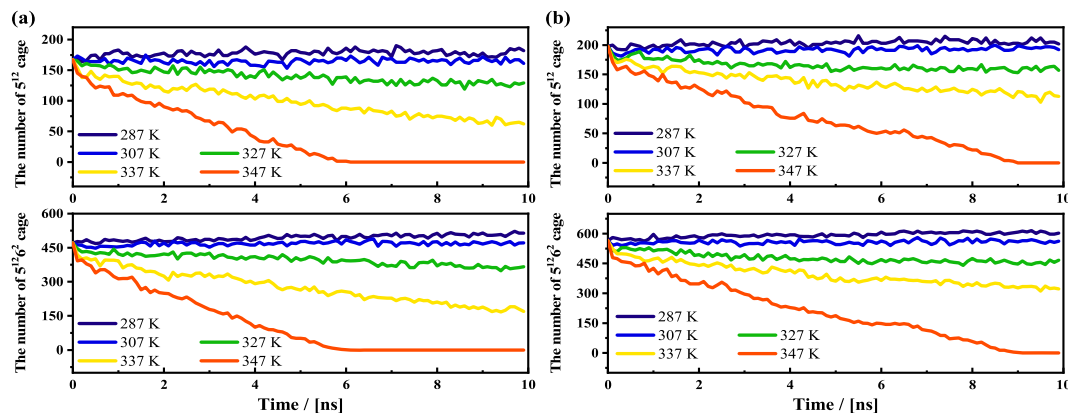


Fig. 5. The number of the two clathrate cages ( $5^{12}$  and  $5^{12}6^2$ ) as a function of time at different temperatures, (a) PHS, (b) MHS.



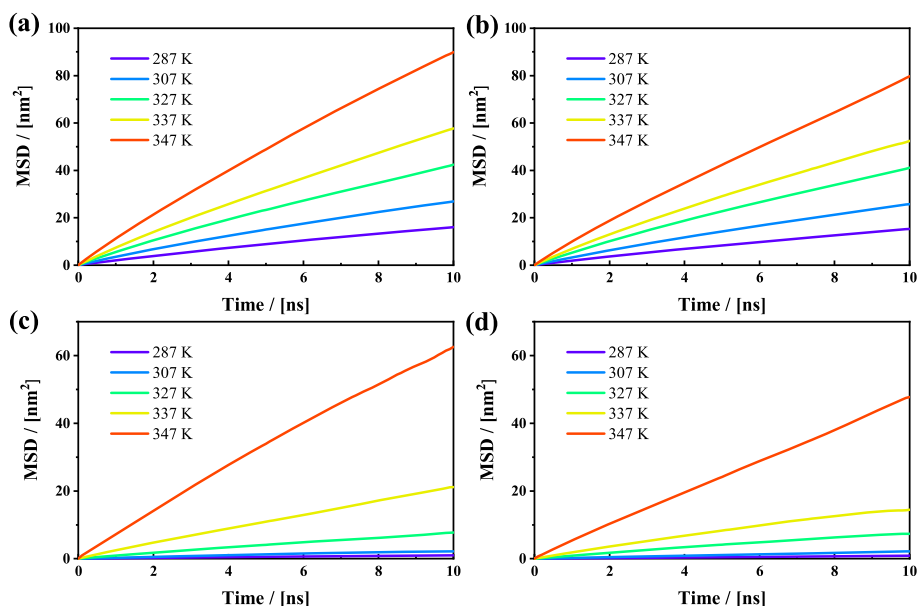


Fig. 6. MSD curves for water ((a) and (b)) and methane ((c) and (d)) molecules in PHS and MHS systems at different temperatures.

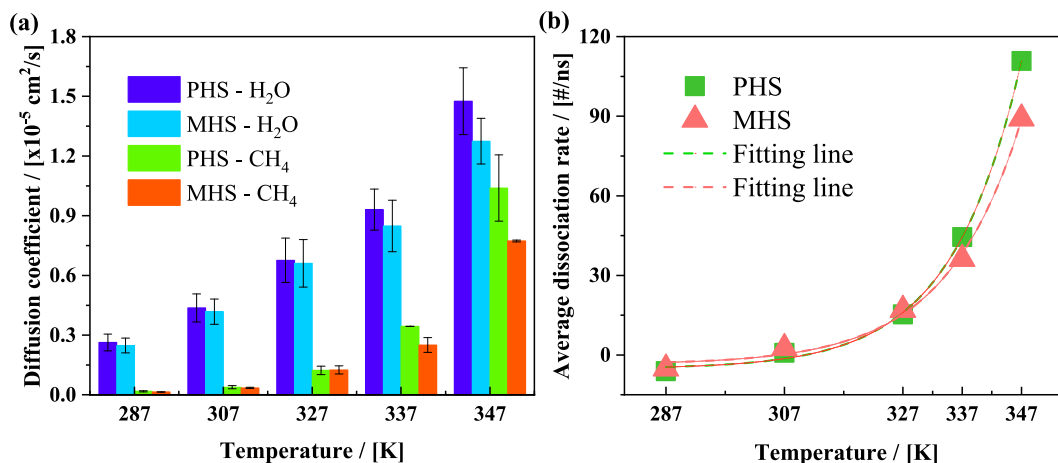


Fig. 7. The diffusion coefficients of water and methane molecules (a), and the average dissociation rate (b) as a function of temperature for the two systems. The rate is fit as an exponential function with the determination coefficient  $R^2$  greater than 0.998.

the PHS and MHS systems at different temperatures (287 K, 327 K, 337 K, and 347 K). At 287 K, both systems exhibit a dynamic stability of the hydrate phase throughout the simulation. By analyzing the entire dissociation process, it can be observed that the hydrate phases dissociate from the outside to the inside in a layer-by-layer manner. This phenomenon aligns with findings from previous studies and suggests a characteristic dissociation pattern for hydrate phases [26,37,89]. Crystals inside the hydrate cluster keep stable until the most outer layer dissociated. This phenomenon is because the mass transfer of guest molecules in the hydrate cages is impeded by outer solid hydrate phase, which can stabilize the cage structure formed by H-bonded network of water molecules.

As shown in Figs. 8 and 9, the shape of the residual hydrate phase seems an elliptical core during the dissociation process in the MHS system (Fig. 9), while in the PHS system (Fig. 6), the water molecules in boundary region between the two hydrate grains exhibit greater instability compared to those in the bulk hydrate phase. As dissociation progresses, water molecules in the solid phase at the grain boundaries rapidly melt from the outside to the inside due to their instability in the y direction. This leads to the caving in of the hydrate phase at the grain

boundary, resulting in a dumbbell shape for the polycrystalline phase (since there are two hydrate grains in the system). This shape increases the interfacial area between the hydrates and water phase compared to that in the monocrystalline hydrate system. As a result, the dissociation process is accelerated with a larger dissociation front surface in the polycrystalline hydrate system at the same temperature and pressure. Although the grain boundary connecting the two hydrate grains decreases during the hydrate dissociation, the two hydrate grains remain bound together through the grain boundary until complete dissociation of the hydrate phase.

At 347 K, the hydrate phase has completely dissociated, and all methane molecules are released from the hydrate phase and diffuse into the surrounding liquid water phase. As a result, nanobubbles are formed due to the low solubility of methane in water [90]. These nanobubbles can be observed in Figs. 8(d) and Fig. 9(d) for both the PHS and MHS systems. These nanobubbles tend to adsorb on the clay surface, forming a small contact angle (less than  $90^\circ$ ), which can be attributed to the hydrophilic nature of the clay surface. This result implies that if thermal stimulation alone is used for hydrate exploitation, particularly in hydrate deposits containing the montmorillonite as the framework, a

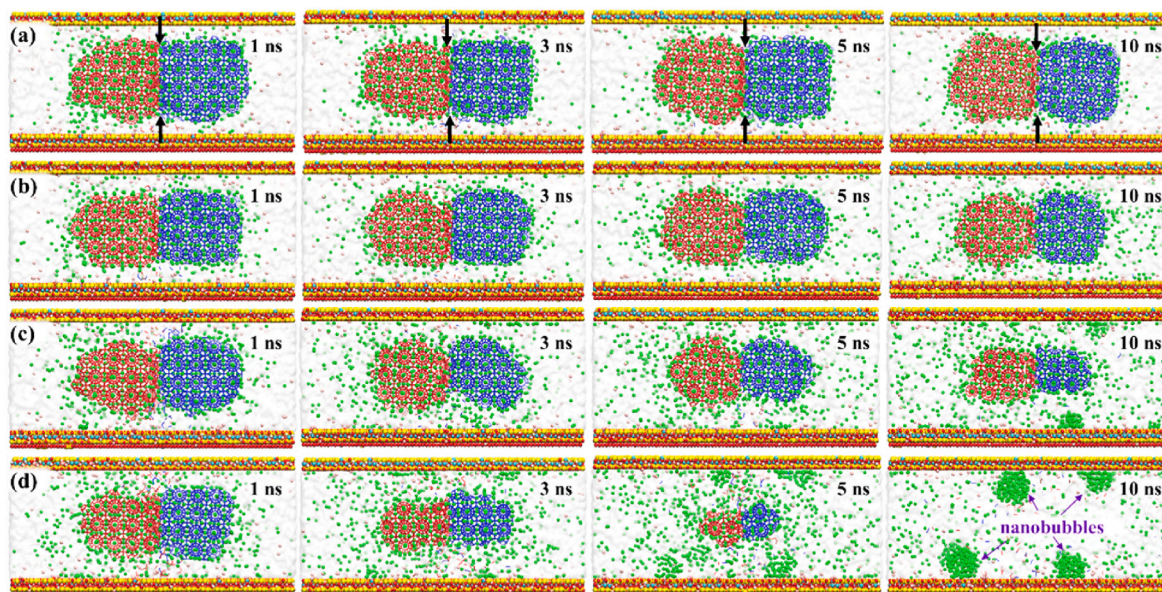


**Fig. 8.** Snapshots of polycrystalline hydrate dissociation in clay nanopores at different temperatures: (a) 287 K, (b) 327 K, (c) 337 K, (d) 347 K. The black arrow indicates the direction of grain boundary recession.

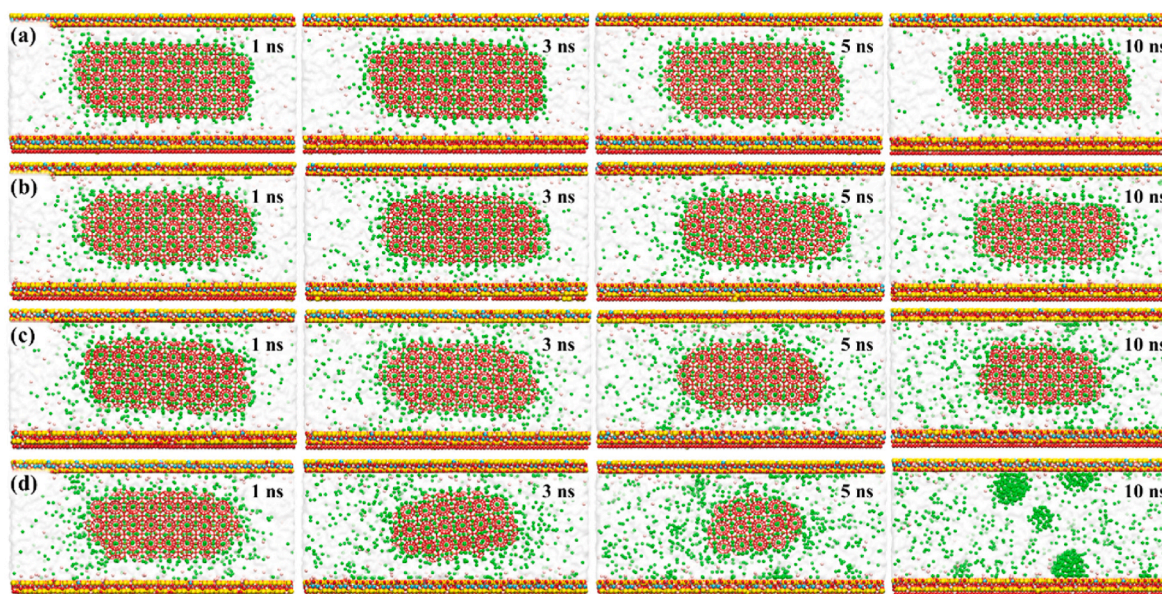


**Fig. 9.** Snapshots of monocrystalline hydrate dissociation in clay nanopores at different temperatures: (a) 287 K, (b) 327 K, (c) 337 K, (d) 347 K.

significant amount of the released gas after hydrate dissociation will remain trapped within the nanopores in the form of nanobubbles, with adsorption occurring on the solid surface. This phenomenon can limit the efficiency of gas extraction from hydrate reservoirs, as the trapped gas is not easily recoverable.

### 3.3. The effect of pressure gradient on hydrate stability

Temperature has a significant effect on the dissociation of poly- and mono-crystalline hydrate. By comparison, depressurization has been more extensively utilized in the extraction of gas from hydrates, as evidenced by the results of previous field trial tests [56–58]. During the depressurization process, a pressure gradient forms along the pores in hydrate reservoirs, resulting in fluid flow through the nanopores (along the x direction in our simulations). As shown in Fig. 5, the number of cages in the hydrate phase maintains a certain dynamic equilibrium at

287 K in a static system, signifying phase stability. However, when pressure gradients are introduced, as seen in Fig. 10, there's a time-dependent change in the number of cages within the clay pore for both the PHS and MHS systems. This decrease in cage count indicates that the hydrate phase loses stability at 287 K. Notably, as the pressure gradient intensifies, the destabilization of the hydrate phase becomes more pronounced, especially when the pressure gradient falls below 50 MPa/nm. This implies that higher pressure gradients have a more significant impact on destabilizing the hydrate phase, leading to a greater reduction in the number of cages within the hydrates.

The large fluctuations in the cage number over time signify the continuous disruption and reconstruction of the hydrogen bonding network framework, which is composed of water molecules. This dynamic process indicates that water molecules, originally in the liquid water phase at the beginning of the simulation, actively participate in the reconstruction of hydrate crystal cages. We quantified the number of

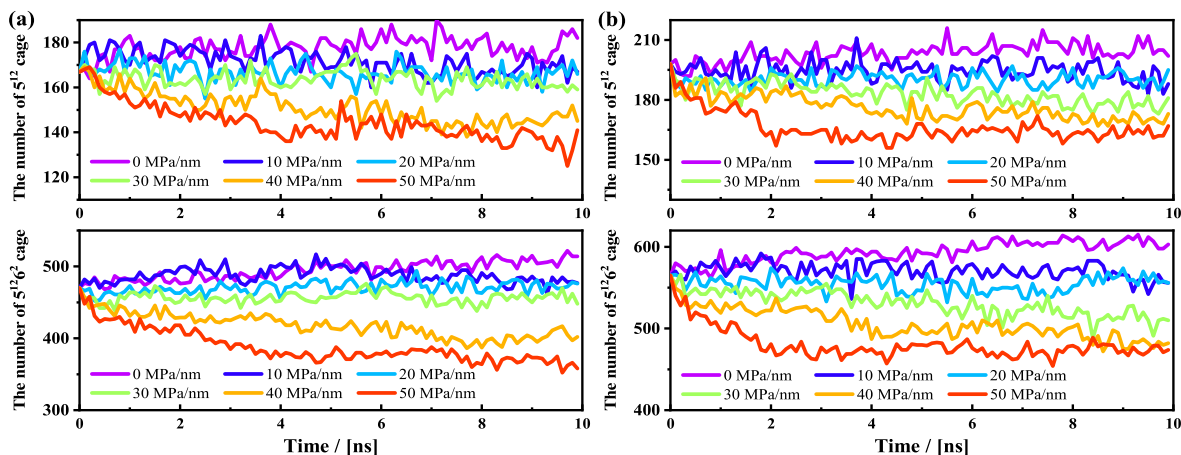


Fig. 10. The number of clathrate cages as a function of time in the flow system at 287 K with different pressure gradients, (a) PHS, (b) MHS.

water molecules involved in the formation of hydrate cages within two distinct categories, both under flow conditions (40 MPa/nm) and static conditions, as illustrated in Fig. 11. One category comprises cages exclusively formed by hydrate water molecules in the initial hydrate system, while the other includes cages formed by all water molecules in the system, encompassing both hydrate and liquid water molecules. The time evolution of the cage number under pressure gradients can be observed in Fig. S4 of the Supporting Information. Regardless of the application of an external driving force, the total number of cages within the system exceeds the initial number of water molecules present in the hydrate. This observation provides compelling evidence that water molecules in the liquid phase actively engage in the hydrate formation process during dissociation. Furthermore, this participation continues throughout the entire dissociation process.

Figs. 12 and 13 present snapshots of the two systems (PHS and MHS) at 10 ns at different pressure gradients. It can be observed that the positions of residual hydrates within the pores vary for the same simulation time for different pressure gradients. This variation is attributed to the fluid velocity driven by the different external forces. The shape of residual hydrates also undergoes changes, particularly for polycrystalline hydrates. At static conditions, the outer surfaces of the hydrate grains exhibit a certain curvature. However, due to the influence of fluid flow, specifically along the flow direction (x direction), the curvature of the outer surface of the hydrate grains gradually diminishes, resulting in a flatter surface shape. This change becomes more pronounced at high-pressure conditions. A lower amount of residual hydrate is observed in the flow system compared to the static system. The reduction in hydrate

formation primarily occurs in the Y-axis direction, while in the X-direction, the dissociation of hydrates is not significant. This indicates that fluid flow primarily affects the hydrates in the Y-axis direction, leading to their dissociation. Due to the fluid flow, residual hydrates not only undergo translation along with the fluid motion but also exhibit a certain degree of rotational movement in the nanopores. Consequently, the fluid flow within the clay pores can be characterized as laminar flow at the given simulation conditions [91].

Fig. 14 illustrates the velocity distribution of water molecules within the clay pore under the influence of the external force. The velocity of water molecules shows a directional movement along the positive x-axis, driven by the pressure gradients. The fluid velocity increases as the pressure gradient increases, as shown in Fig. 14(a) for the PHS system and Fig. 14(b) for the MHS system. The velocity distributions exhibit a plateau near the center of the pore and are almost symmetrical along the Y direction. The velocity of water near the clay surface is lower than that in the pore center. This can be attributed to the interaction between the hydrophilic clay surface and water molecules, which leads to a slower velocity of water near the solid surface. In Fig. 14(c), the average velocity of water in the systems and in the residual hydrate phases is shown. It is observed that the average velocity of water in the residual hydrate phase is higher than that in the overall system. This phenomenon may be caused by the lower velocity of water near the solid surface, as water molecules on the clay surface are influenced by the interaction with the hydrophilic solid surface. The results also indicate that the fluid flow rate in the nanopore increases non-linearly with the pressure gradient, suggesting the presence of non-Darcy flow behavior in the

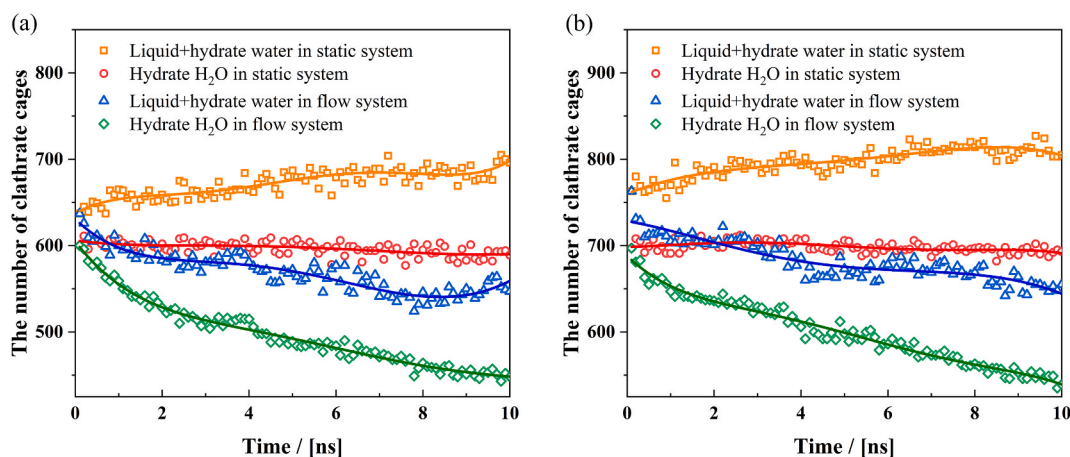


Fig. 11. Time variation of two types of hydrate cage numbers constructed by water in the static system and in the flow system (driven by pressure gradient of 40 MPa/nm).

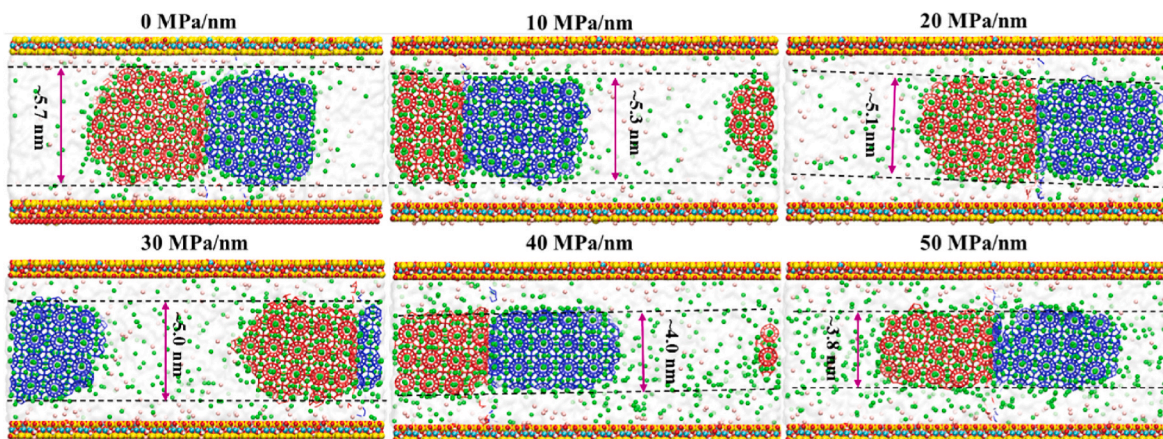


Fig. 12. Snapshots of hydrate dissociation in 10.0 ns in clay pore for the PHS system at 287 K for different pressure gradients.

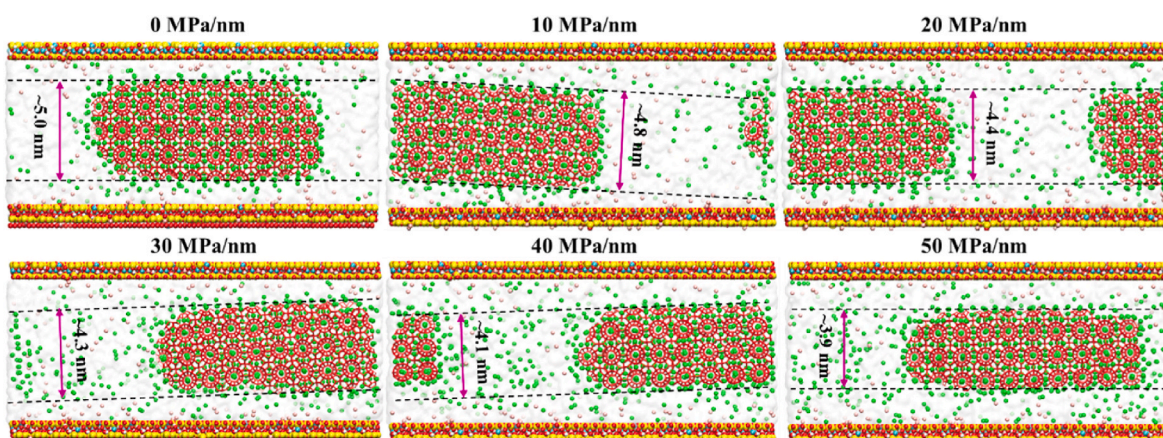


Fig. 13. Snapshots of hydrate dissociation in 10.0 ns in clay pore for the MHS system at 287 K for different pressure gradients.

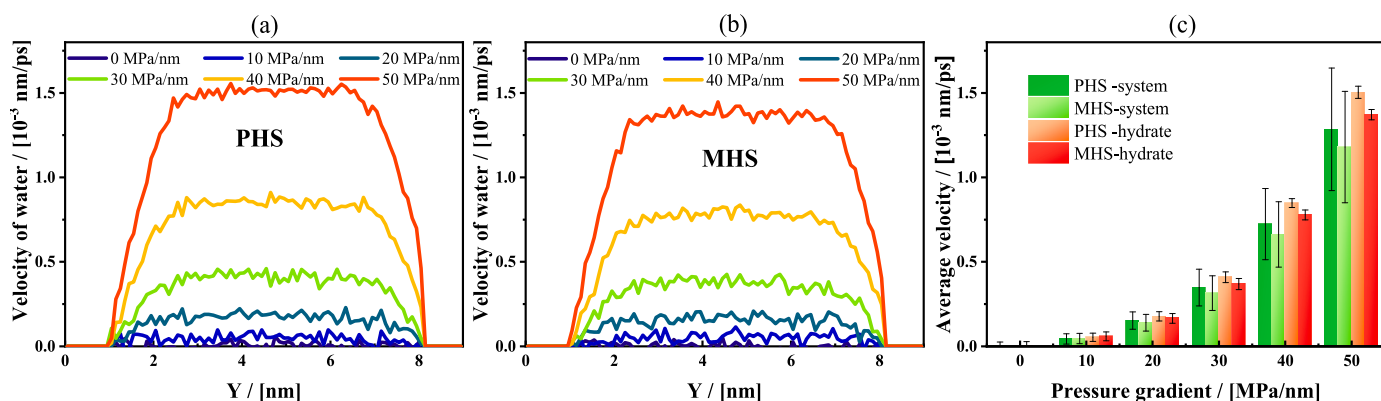


Fig. 14. The velocity profiles of water molecules in clay pore for different pressure gradients for the (a) PHS and (b) MHS systems at 287 K, and (c) the average velocity of water molecules in pore and the hydrate phase for the both systems.

simulation. This means that the fluid flow does not strictly follow Darcy's law (which describes flow through porous media at laminar flow conditions) [92].

Fig. 15(a) presents the average number of hydrogen bonds between water molecules in the system. This is an indicator of the stability of the hydrate cluster. As the pressure gradients increase from 0 to 50 MPa/nm, the average number of H-bonds of water molecules decreases. This suggests that the system becomes less stable in a flow system, indicating a disruption of the H-bond network between water molecules. Fig. 15(b)

shows the average number of H-bonds between water molecules and the clay surface. When the pressure gradients are below 50 MPa/nm, the average number of hydrogen bonds remains relatively constant. This indicates that the external forces acting on water molecules are not strong enough to overcome the adhesive forces between water and the solid surface. As a result, water molecules on the surface of the solid (clay) remain adhered to the surface, while the hydrate phase in the center of the clay pore experiences accelerated dissociation due to the external force. In Figs. 12 and 13, it is observed that the phase change of

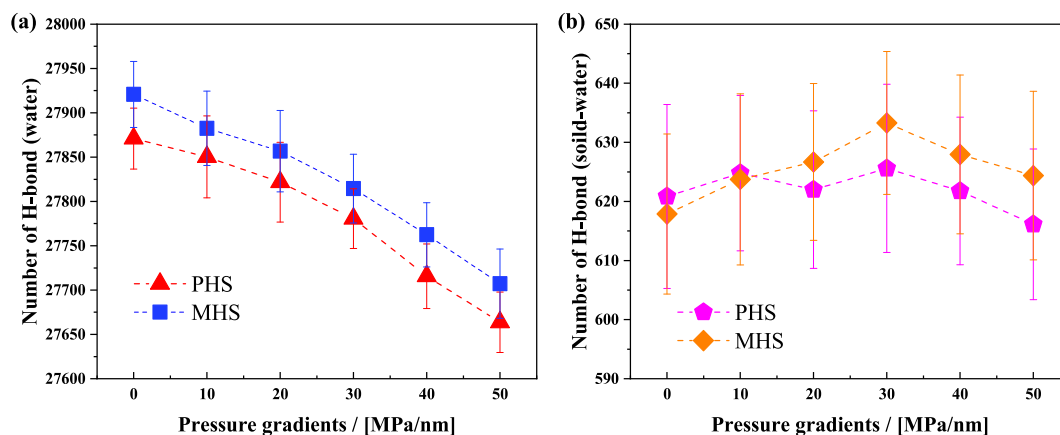


Fig. 15. The number of H-bonds between (a) water molecules in the systems and (b) between clay surface and water molecules.

hydrate primarily occurs in the Y direction due to the fluid flow. This can be attributed to the velocity difference between the liquid water layer and the hydrate phase. The viscous flow causes the water molecules on the surface of the hydrate to become unstable and separate from the hydrate structure, thereby transitioning into the liquid phase. The velocity of water molecules within the hydrate structure exhibits inconsistency compared to the surrounding water molecules. Particularly, there is a significant disparity in velocity between water molecules in the vertical direction, while the discrepancy is relatively minor in the parallel direction. This variation in velocity distribution is considered a significant factor contributing to the dissociation of hydrate along the vertical flow direction.

#### 3.4. Hydrate dissociation in a flow system and nanobubble evolution

At 347 K, the hydrate phase completely dissociates in both static and flow systems. In the flow system, the dissociation of hydrate also occurs in a layer-by-layer manner with a significant dissociation rate. The snapshots of hydrate dissociation at 347 K for the PHS and MHS systems with different pressure gradients are shown in Figs. S5 and S6 of the Supporting Information, respectively. At the same dissociation temperature, the dissociation rate of hydrate in pore is further accelerated in the flow system, as shown in Fig. 16. In the polycrystalline system, water molecules at grain boundaries are more unstable compared to those in the bulk phase, making them more prone to dissociation. Thus, the polycrystalline hydrate dissociates faster than the monocrystalline hydrate at the same conditions. The simulations indicate that the polycrystalline hydrate dissociates most rapidly when the pressure gradient

is 10 MPa/nm. When applying a pressure gradient, simulations have observed the potential occurrence of fractures at grain boundaries, resulting in the formation of two separate hydrated crystal grains. This phenomenon leads to an increase in the dissociation surface area and accelerates the dissociation rate, as shown in Fig. 17. In other cases, the hydrated crystal grains do not separate; they remain bonded together through hydrogen bonding interactions.

At 347 K, the dissociation of the hydrate cluster occurs rapidly within a few nanoseconds. This leads to the release of methane from the solid hydrate phase and the formation of nanobubbles due to the low solubility of methane in the water phase. The observations from Figs. 8 and 9 indicate that surface nanobubbles form in a static system. However, in flow systems, nanobubbles do not form on the clay surface. Instead, most of the released methane aggregates in the liquid water phase and moves along with the fluid flow (Figs. 18 and 19). Within the clay nanopore, nanobubbles are frequently observed near the center of the pores in flow systems. This occurrence is primarily attributed to the laminar flow within the nanoscale pores, as confirmed by the velocity distribution along the Y-axis inside the pores in Fig. S7. As the fluid approaches the center of the pore, the flow velocity increases while the pressure decreases. Consequently, dissolved gases in the liquid phase tend to migrate towards the center of the pore, resulting in the formation of nanobubbles in the liquid phase. It is important to note that for high flow velocity conditions, (e.g., 20 MPa/nm), the shape of nanobubbles undergoes deformation, taking on a triangular cone shape along the direction of movement. This indicates the dynamic behavior of nanobubbles influenced by the fluid flow. In practical gas extraction processes, the formation of surface nanobubbles in a static system is

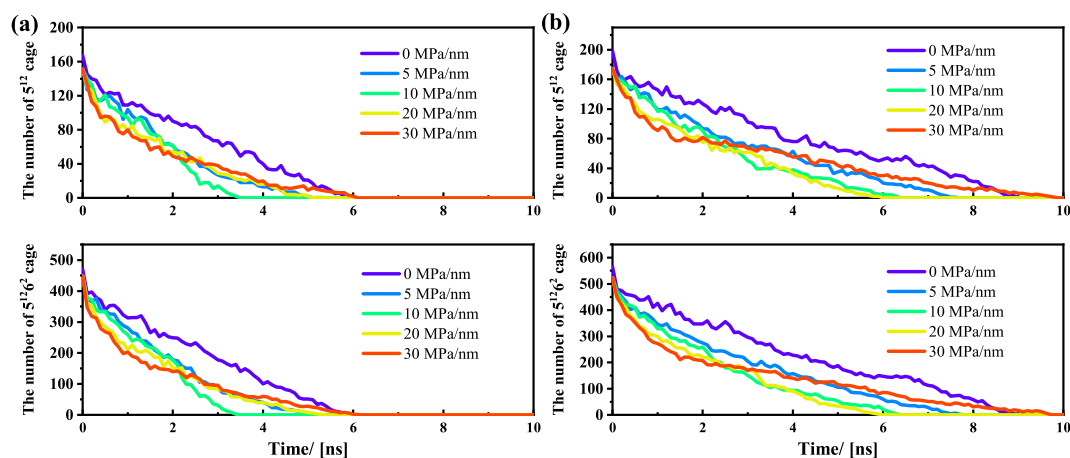


Fig. 16. Time evolution of the number of clathrate cages in the flow system for different pressure gradients at 347 K, (a) PHS, (b) MHS.

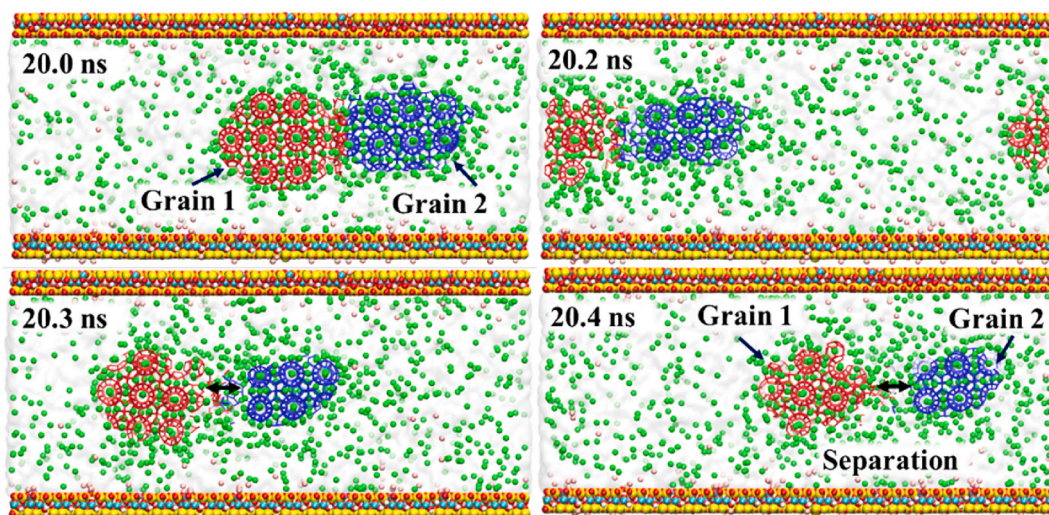


Fig. 17. Snapshots of hydrate dissociation for the polycrystal hydrate system at 10 MPa/nm.

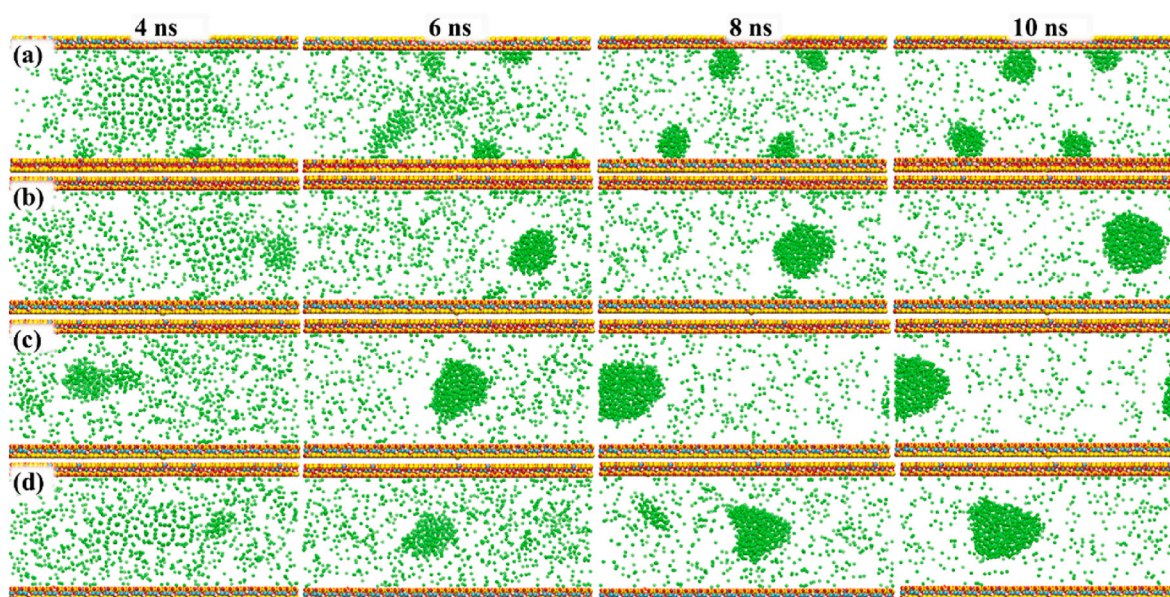


Fig. 18. Snapshots of nanobubble evolution for the poly-crystalline hydrate dissociation system at different pressure gradients (a) 0 MPa/nm; (b) 5 MPa/nm; (c) 10 MPa/nm; (d) 20 MPa/nm.

unfavorable for the transportation of dissociated gas, which can have a negative impact on the efficiency of hydrate extraction through heating. During depressurization, nanobubbles form in the liquid phase and move with the fluid flow. The combination of thermal stimulation and depressurization can increase the efficiency of gas production from hydrate reservoirs. These findings emphasize the importance of considering nanobubble behavior in the design and optimization of gas extraction methods from hydrate reservoirs, especially in relation to the effects of fluid flow and depressurization conditions.

#### 4. Summary and conclusions

This paper focuses on the phase transition process of methane hydrates in marine sediments induced by thermal stimulation and depressurization gas production methods, respectively. Two multi-phase molecular initial configurations have been created to study the behavior of poly- and mono-crystalline methane hydrate dissociation in slit-shaped Na-montmorillonite clay nanopores. Classical MD and EF-

NEMD simulations are applied to static and dynamic scenarios, respectively. The main conclusions are summarized as follows:

1. The hydrate dissociation process proceeds layer by layer, starting from the surface. With rising temperature, the thermodynamic instability of water and methane molecules in hydrates increases, leading to a greater destabilization of the hydrate structure and an accelerated dissociation.
2. In a fluid environment, the instability of hydrates is enhanced. The hydrophilic solid surface interacts with surface-bound water molecules, causing a reduction in the velocity of these molecules. The resulting difference in velocity between surface-bound water and the hydrate phase leads to viscous flow and disrupts the hydrate's surface water molecule structure. The interaction between the solid surface and water molecules significantly impacts hydrate phase stability, and this destabilization effect is further amplified under specific pressure gradients.

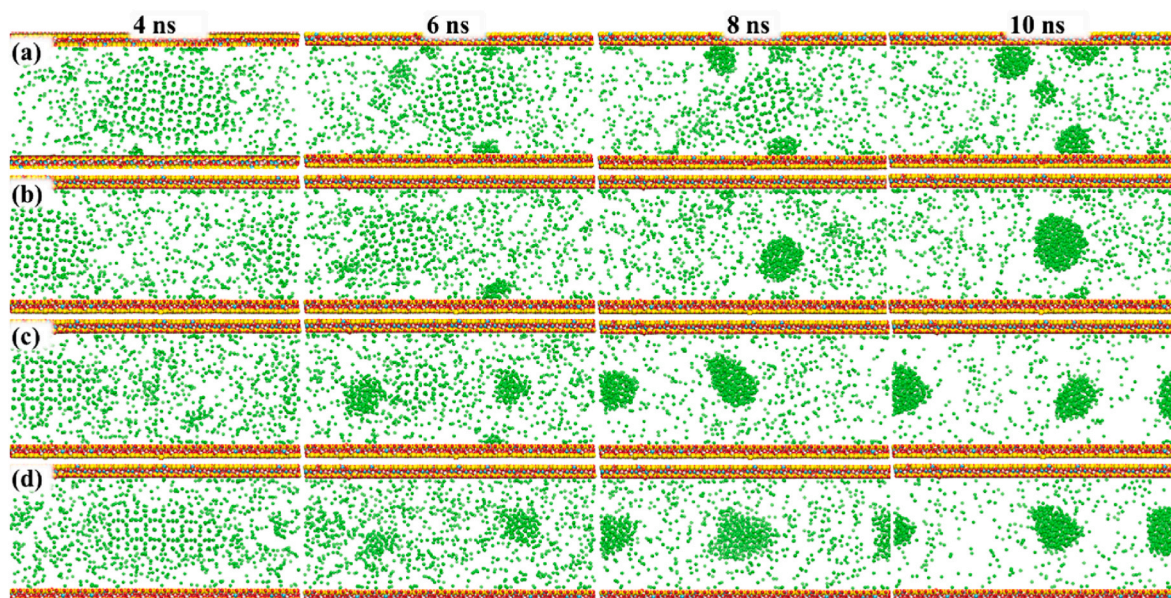


Fig. 19. Snapshots of nanobubble evolution for the mono-crystalline hydrate dissociation system at different pressure gradients (a) 0 MPa/nm; (b) 5 MPa/nm; (c) 10 MPa/nm; (d) 20 MPa/nm.

- In poly-crystalline hydrate systems, grain boundary hydrogen bonding is less stable than in the bulk phase, increasing susceptibility to dissociation. This creates new dissociation surfaces, resulting in a higher dissociation rate compared to mono-crystalline hydrate systems under the same conditions.
- Laminar flow promotes the formation of nanobubbles in the fluid. Unlike the surface nanobubbles observed under static heating conditions, these nanobubbles can enhance the efficiency of gas production from hydrate.
- Due to external forces, fracture events have been observed in poly-crystalline hydrates at grain boundaries. These fractures lead to the formation of two separate hydrate crystal grains, thereby accelerating the dissociation process.

Due to limitations in computational resources, several approximations were made in this study. For instance, only two grains are considered in the polycrystalline structure, and large pressure gradients are applied. These approximations deviate from the actual conditions. However, this study simulates the dissociation behavior of poly-crystalline and monocrystalline hydrates in clay mineral pores at both dynamic and static conditions. It significantly contributes to our understanding of the molecular mechanisms of grain boundaries and fluid interactions on hydrate dissociation. This research enhances our fundamental scientific understanding of hydrate extraction from porous media.

#### CRedit authorship contribution statement

**Bin Fang:** Data curation, Formal analysis, Investigation, Methodology, Validation, Visualization, Writing - original draft. **Tao Lü:** Writing - review & editing. **Wei Li:** Writing - review & editing. **Othonas A. Moultos:** Writing - review & editing. **Thijs J.H. Vlugt:** Writing - review & editing. **Fulong Ning:** Funding acquisition, Resources, Writing - review & editing.

#### Declaration of competing interest

The authors declare that they have no known competing financial interests or personal relationships that could have appeared to influence the work reported in this paper.

#### Data availability

Data will be made available on request.

#### Acknowledgment

This work was supported by the National Natural Science Foundation of China (Grants 42206235 and 42225207), and the International Postdoctoral Exchange Fellowship Program (No. PC2021073).

#### Appendix A. Supplementary data

Supplementary data to this article can be found online at <https://doi.org/10.1016/j.energy.2023.129755>.

#### References

- [1] Sloan ED. Fundamental principles and applications of natural gas hydrates. *Nature* 2003;426(6964):353–63.
- [2] Boswell R. Is Gas hydrate energy within reach? *Science* 2009;325(5943):957–8.
- [3] Collett T, Bahk JJ, Baker R, Boswell R, Divins D, Frye M, et al. Methane hydrates in nature—current knowledge and challenges. *J Chem Eng Data* 2014;60(2):319–29.
- [4] Sloan ED, Koh CA. Clathrate hydrates of natural gases. *Crc Press*; 2007.
- [5] Nandanwar MS, Anderson BJ, Ajayi T, Collett TS, Zyrianova MV. Evaluation of gas production potential from gas hydrate deposits in National Petroleum Reserve Alaska using numerical simulations. *J Nat Gas Sci Eng* 2016;36:760–72.
- [6] Li XS, Xu CG, Zhang Y, Ruan XK, Li G, Wang Y. Investigation into gas production from natural gas hydrate: a review. *J Applied Energy* 2016;172(Jun.15):286–322.
- [7] Florusse LJ, Peters CJ, Schoonman J, Hester KC, Koh CA, Dec SF, et al. Stable low-pressure hydrogen clusters stored in a binary clathrate hydrate. *Science* 2004;306(5695):469–71.
- [8] Yamamoto K, Boswell R, Collett TS, Dallimore SR, Lu H. Review of past gas production attempts from subsurface gas hydrate deposits and necessity of long-term production testing. *Energy Fuels* 2022;36(10):5047–62.
- [9] Bhattacharjee G, Kumar A, Sakpal T, Kumar R. Carbon dioxide sequestration: influence of porous media on hydrate formation kinetics. *ACS Sustainable Chem Eng* 2015;3(6):1205–14.
- [10] Fang B, Ning F, Hu S, Guo D, Ou W, Wang C, et al. The effect of surfactants on hydrate particle agglomeration in liquid hydrocarbon continuous systems: a molecular dynamics simulation study. *RSC Adv* 2020;10(52):31027–38.
- [11] Lee H, Lee JW, Kim DY, Park J, Seo YT, Zeng H, et al. Tuning clathrate hydrates for hydrogen storage. *Nature* 2005;434(7034):743–6.
- [12] Babu P, Nambiar A, He TB, Karimi IA, Lee JD, Englezos P, et al. A review of clathrate hydrate based desalination to strengthen energy-water nexus. *ACS Sustainable Chem Eng* 2018;6(7):8093–107.
- [13] Dong HS, Wang JQ, Xie ZX, Wang B, Zhang LX, Shi Q. Potential applications based on the formation and dissociation of gas hydrates. *Renewable Sust Energy Rev* 2021;143:110928.

- [14] Kumar A, Veluswamy HP, Kumar R, Linga P. Direct use of seawater for rapid methane storage via clathrate (sII) hydrates. *Appl Energy* 2019;235:21–30.
- [15] XiaoSen L, ChunGang X, Yu Z, XuKe R, Gang L, Yi W. Investigation into gas production from natural gas hydrate: a review. *Appl Energy* 2016;172:286–322.
- [16] Kim HC, Bishnoi PR, Heidemann RA, Rizvi SSH. Kinetics of methane hydrate decomposition. *Chem Eng Sci* 1987;42(7):1645–53.
- [17] Jamaluddin AKM, Kalogerakis N, Bishnoi PR. Modelling of decomposition of a synthetic core of methane gas hydrate by coupling intrinsic kinetics with heat transfer rates. *Can J Chem Eng* 1989;67(6):948–54.
- [18] Goel N, Shah S, Wiggins M. Analytical modeling of gas recovery from in situ hydrates dissociation. *J Petrol Sci Eng* 2001;29(2):115–27.
- [19] Yang H, Jayaatmaja K, Dejam M, Tan SP, Adidharma H. Phase transition and criticality of methane confined in nanopores. *Langmuir* 2022;38(6):2046–54.
- [20] Sarupria S, Debenedetti PG. Homogeneous nucleation of methane hydrate in microsecond molecular dynamics simulations. *J Phys Chem Lett* 2012;3(20):2942–7.
- [21] Walsh MR, Beckham GT, Koh CA, Sloan ED, Wu DT, Sum AK. Methane hydrate nucleation rates from molecular dynamics simulations: effects of aqueous methane concentration, interfacial curvature, and system size. *J Phys Chem C* 2011;115(43):21241–8.
- [22] DeFever RS, Sarupria S. Surface chemistry effects on heterogeneous clathrate hydrate nucleation: a molecular dynamics study. *J Chem Thermodyn* 2018;117:205–13.
- [23] Fang B, Lü T, Ning F, Pang J, He Z, Sun J. Facilitating gas hydrate dissociation kinetics and gas migration in clay interlayer by surface cations shielding effects. *Fuel* 2022;318:123576.
- [24] Bagherzadeh SA, Englezos P, Alavi S, Ripmeester JA. Molecular modeling of the dissociation of methane hydrate in contact with a silica surface. *J Phys Chem B* 2012;116(10):3188–97.
- [25] Liao B, Wang J, Han X, Wang R, Lv K, Bai Y, et al. Microscopic molecular insights into clathrate methane hydrates dissociation in a flowing system. *Chem Eng J* 2022;430:133098.
- [26] Fang B, Ning F, Ou W, Wang D, Zhang Z, Yu Y, et al. The dynamic behavior of gas hydrate dissociation by heating in tight sandy reservoirs: a molecular dynamics simulation study. *Fuel* 2019;258:116106.
- [27] Wu Z, Liu W, Zheng J, Li Y. Effect of methane hydrate dissociation and reformation on the permeability of clayey sediments. *Appl Energy* 2020;261:114479.
- [28] Cheng C, Zhao J, Yang M, Liu W, Wang B, Song Y. Evaluation of gas production from methane hydrate sediments with heat transfer from over-underburden layers. *Energy Fuels* 2015;29(2):1028–39.
- [29] Yang X, Sun CY, Yuan Q, Ma PC, Chen GJ. Experimental study on gas production from methane hydrate-bearing sand by hot-water cyclic injection. *Energy Fuels* 2010;24(11):5912–20.
- [30] Jung JW, Jang J, Santamarina JC, Tsouris C, Phelps TJ, Rawn CJ. Gas production from hydrate-bearing sediments: the role of fine particles. *Energy Fuels* 2012;26(1):480–7.
- [31] Zhang Z, Li C, Ning F, Liu L, Wang DD, et al. Pore fractal characteristics of hydrate bearing sands and implications to the saturated water permeability. *J Geophys Res Solid Earth* 2020;125(3):e2019JB018721.
- [32] Ta XH, Yun TS, Mhunthan B, Kwon TH. Observations of pore-scale growth patterns of carbon dioxide hydrate using X-ray computed microtomography. *G-cubed* 2015;16(3):912–24.
- [33] Lei L, Seol Y, Choi JH, Kneafsey T. Pore habit of methane hydrate and its evolution in sediment matrix – laboratory visualization with phase-contrast micro-CT. *Mar Petrol Geol* 2019;104:451–67.
- [34] Kuang Y, Zhang L, Song Y, Yang L, Zhao J. Quantitative determination of pore-structure change and permeability estimation under hydrate phase transition by NMR. *AIChE J* 2020;66:16859.
- [35] i Y, Hou J, Liu Y, Du Q. Study on Formation and Dissociation of Methane Hydrate in Sandstone Using Low-Field Nuclear Magnetic Resonance Technology. *Conference Study on Formation and Dissociation of Methane Hydrate in Sandstone Using Low-Field Nuclear Magnetic Resonance Technology* 2020;84430. V011T11A017.
- [36] Ge X, Liu J, Fan Y, Xing D, Deng S, Cai J. Laboratory investigation into the formation and dissociation process of gas hydrate by low-field NMR technique. *J Geophys Res Solid Earth* 2018;123(5):3339–46.
- [37] Baez LA, Clancy P. Computer-simulation of the crystal-growth and dissolution of natural-gas hydrates. *Int Conf Natural Gas Hydrates* 1994;715:177–86.
- [38] Reshadi P, Modarress H, Dabir B, Amjad-Iranagh S. A study on dissociation of sII krypton hydrate and the effect of hydrocarbon guest molecules as stabilizer by molecular dynamics simulation. *Phase Transitions* 2017;90(11):1128–42.
- [39] Liu Y, Zhao JJ, Xu JC. Dissociation mechanism of carbon dioxide hydrate by molecular dynamic simulation and ab initio calculation. *Comput Theor Chem* 2012;991:165–73.
- [40] Yan KF, Li XS, Chen ZY, Li B, Xu CG. Molecular dynamics simulation of methane hydrate dissociation by depressurisation. *Mol Simulat* 2013;39(4):251–60.
- [41] English NJ, Johnson JK, Taylor CE. Molecular-dynamics simulations of methane hydrate dissociation. *J Chem Phys* 2005;123(24):244503.
- [42] Tsimpanogiannis IN, Costandy J, Kastanidis P, El Meragawi S, Michalis VK, Papadimitriou NI, et al. Using clathrate hydrates for gas storage and gas-mixture separations: experimental and computational studies at multiple length scales. *Mol Phys* 2018;116(15–16):2041–60.
- [43] Michalis VK, Economou IG, Stubos AK, Tsimpanogiannis IN. Phase equilibria molecular simulations of hydrogen hydrates via the direct phase coexistence approach. *J Chem Phys* 2022;157(15).
- [44] Bagherzadeh SA, Alavi S, Ripmeester J, Englezos P. Formation of methane nanobubbles during hydrate decomposition and their effect on hydrate growth. *J Chem Phys* 2015;142(21):214701.
- [45] Iwai Y, Nakamura H, Arai Y, Shimoyama Y. Analysis of dissociation process for gas hydrates by molecular dynamics simulation. *Mol Simulat* 2010;36(3):246–53.
- [46] Yagasaki T, Matsumoto M, Andoh Y, Okazaki S, Tanaka H. Dissociation of methane hydrate in aqueous NaCl solutions. *J Phys Chem B* 2014;118(40):11797–804.
- [47] Fang B, Moulton OA, Lü T, Sun J, Liu Z, Ning F, et al. Effects of nanobubbles on methane hydrate dissociation: a molecular simulation study. *Fuel* 2023;345:128230.
- [48] Chen J, Liu C, Zhang Z, Wu N, Liu C, Ning F, et al. Molecular study on the behavior of methane hydrate decomposition induced by ions electrophoresis. *Fuel* 2022;307:121866.
- [49] Yagasaki T, Matsumoto M, Andoh Y, Okazaki S, Tanaka H. Effect of bubble formation on the dissociation of methane hydrate in water: a Molecular dynamics study. *J Phys Chem B* 2014;118(7):1900–6.
- [50] Wang LB, Cui JL, Sun CY, Ma QL, Fan SS, Wang XH, et al. Review on the applications and modifications of the Chen–Guo model for hydrate formation and dissociation. *Energy Fuels* 2021;35(4):2936–64.
- [51] Yu X, Li Gang, Li Q, Li X, Zhang Y, Pang W, et al. Experimental simulation of gas hydrate decomposition in porous sediment. *Sci China Earth Sci* 2013;43(3):400–5.
- [52] Stern LA, Lorensen TD, Pinkston JC. Gas hydrate characterization and grain-scale imaging of recovered cores from the mount elbert gas hydrate stratigraphic test well, Alaska north slope. *Mar Petrol Geol* 2011;28(2):394–403.
- [53] Li W, Pang J, Peng L, Fang B, Ou W, Tao Z, et al. Microscopic insights into the effects of anti-agglomerant surfactants on surface characteristics of tetrahydrofuran hydrate. *Energy Fuels* 2023;37(5):3741–51.
- [54] Wu J, Ning F, Trinh TT, Kjelstrup S, Flugt TJH, He J, et al. Mechanical instability of monocrystalline and polycrystalline methane hydrates. *Nat Commun* 2015;6(1):8743.
- [55] Zhang Z, Kusalik PG, Guo GJ, Ning F, Wu N. Insight on the stability of polycrystalline natural gas hydrates by molecular dynamics simulations. *Fuel* 2021;289(9):119946.
- [56] Ning F, Chen Q, Sun J, Wu X, Cui G, Mao P, et al. Enhanced gas production of silty clay hydrate reservoirs using multilateral wells and reservoir reformation techniques: numerical simulations. *Energy* 2022;254:124220.
- [57] Cao X, Sun J, Qin F, Ning F, Mao P, Gu Y, et al. Numerical analysis on gas production performance by using a multilateral well system at the first offshore hydrate production test site in the Shenhu area. *Energy* 2023;270:126690.
- [58] Sun J, Zhang L, Ning F, Lei H, Liu T, Hu G, et al. Production potential and stability of hydrate-bearing sediments at the site GMGS3-W19 in the South China Sea: a preliminary feasibility study. *Mar Petrol Geol* 2017;86:447–73.
- [59] Downs RT, Hall-Wallace M. The American Mineralogist crystal structure database. *Am Mineral* 2003;88(1):247–50.
- [60] Yan KF, Li XS, Xu CG, Lv QN, Ruan XK. Molecular dynamics simulation of the intercalation behaviors of methane hydrate in montmorillonite. *J Mol Model* 2014;20:2311.
- [61] Loewenstein W. The distribution of aluminum in the tetrahedra of silicates and aluminates. *Am Mineral* 1954;39(1–2):92–6.
- [62] Takeuchi F, Hiratsuka M, Ohmura R, Alavi S, Sum AK, Yasuoka K. Water proton configurations in structures I, II, and H clathrate hydrate unit cells. *J Chem Phys* 2013;138(12):124504.
- [63] He Z, Linga P, Jiang J. CH<sub>4</sub> hydrate formation between silica and graphite surfaces: insights from microsecond molecular dynamics simulations. *Langmuir* 2017;33(43):11956–67.
- [64] Bai DS, Chen GJ, Zhang XR, Sum AK, Wang WC. How properties of solid surfaces modulate the nucleation of gas hydrate. *Sci Rep-Uk* 2015;5.
- [65] Liang S, Kusalik PG. The nucleation of gas hydrates near silica surfaces. *Can J Chem* 2015;93(8):791–8.
- [66] Chaouachi M, Falenty A, Sell K, Enzmann F, Kersten M, Habertur D, et al. Microstructural evolution of gas hydrates in sedimentary matrices observed with synchrotron X-ray computed tomographic microscopy. *G-cubed* 2015;16(6):1711–22.
- [67] Abascal JLF, Sanz E, García Fernández R, Vega C. A potential model for the study of ices and amorphous water: TIP4P/Ice. *J Chem Phys* 2005;122(23).
- [68] Martin MG, Siepmann JI. Transferable potentials for phase equilibria. 1. United-atom description of n-alkanes. *J Phys Chem B* 1998;102(14):2569–77.
- [69] Cygan RT, Liang J-J, Kalinichev AG. Molecular models of hydroxide, oxyhydroxide, and clay phases and the development of a general force field. *J Phys Chem B* 2004;108(4):1255–66.
- [70] Jensen L, Thomsen K, von Solms N, Wierchowksi S, Walsh MR, Koh CA, et al. Calculation of liquid water–hydrate–methane vapor phase equilibria from molecular simulations. *J Phys Chem B* 2010;114(17):5775–82.
- [71] Mi F, He Z, Fang B, Ning F, Jiang G. Molecular insights into the effects of surface property and pore size of non-swelling clay on methane hydrate formation. *Fuel* 2021:122607.
- [72] Kyung D, Lim H-K, Kim H, Lee W. CO<sub>2</sub> hydrate nucleation kinetics enhanced by an organo-mineral complex formed at the montmorillonite-water interface. *Environ Sci Technol* 2015;49:1197–205.
- [73] Cygan RT, Liang JJ, Kalinichev AG. Molecular models of hydroxide, oxyhydroxide, and clay phases and the development of a general force field. *J Phys Chem B* 2004;108(4):1255–66.
- [74] Ratner MA. Understanding molecular simulation: from algorithms to applications, by daan frenkel and berend smit. *Phys Today* 1997;50(7):66.
- [75] Lennard-Jones JE. Cohesion. *Proceedings of the Royal Society* 1931;43(5):461–82.
- [76] Allen MP, Tildesley DJ. *Computer simulation of liquids*. 1987.



- [77] Essmann U, Perera L, Berkowitz ML, Darden T, Lee H, Pedersen LG. A smooth particle mesh Ewald method. *J Chem Phys* 1995;103(19):8577–93.
- [78] Hess B, Kutzner C, van der Spoel D, Lindahl E. Gromacs 4: algorithms for highly efficient, load-balanced, and scalable molecular simulation. *J Chem Theor Comput* 2008;4(3):435–47.
- [79] Abraham MJ, Murtola T, Schulz R, Páll S, Smith JC, Hess B, et al. GROMACS: high performance molecular simulations through multi-level parallelism from laptops to supercomputers 2015;1–2(C):19–25.
- [80] Jacobson LC, Hujo W, Molinero V. Thermodynamic stability and growth of guest-free clathrate hydrates: a low-density crystal phase of water. *J Phys Chem B* 2009;113(30):10298–307.
- [81] Zimmermann K. Oral - all purpose molecular mechanics simulator and energy minimizer. *J Comput Chem* 1991;12(3):310–9.
- [82] Qin X, Liang Q, Ye J, Yang L, Qiu H, Xie W, et al. The response of temperature and pressure of hydrate reservoirs in the first gas hydrate production test in South China Sea. *Appl Energy* 2020;278:115649.
- [83] Bussi G, Donadio D, Parrinello M. Canonical sampling through velocity rescaling. *J Chem Phys* 2007;126(1).
- [84] Parrinello M. Polymorphic transitions in single crystals: a new molecular dynamics method. *J Appl Phys* 1981;52(12):7182–90.
- [85] Xu J, Zhan S, Wang W, Su Y, Wang H. Molecular dynamics simulations of two-phase flow of n-alkanes with water in quartz nanopores. *Chem Eng J* 2022;430:132800.
- [86] Zhan S, Su Y, Jin Z, Wang W, Li L. Effect of water film on oil flow in quartz nanopores from molecular perspectives. *Fuel* 2020;262:116560.
- [87] Rodger PM, Forester TR, et al. Simulations of the methane hydrate/methane gas interface near hydrate forming conditions conditions 1996;116(1–2):326–32.
- [88] Johnson CA. Generalization of the gibbs-thomson equation. *Surf Sci* 1965;3(5):429–44.
- [89] Ding LY, Geng CY, Zhao YH, Wen H. Molecular dynamics simulation on the dissociation process of methane hydrates. *Mol Simulat* 2007;33(12):1005–16.
- [90] Fang B, Habibi P, Moulton OA, Lü T, Ning F, Vlugt TJH. Solubilities and self-diffusion coefficients of light n-alkanes in NaCl solutions at the temperature range (278.15–308.15) K and pressure range (1–300) bar and thermodynamics properties of their corresponding hydrates at (150–290) K and (1–7000) bar. *J Chemical Eng Data* 2023.
- [91] Holland DM, Lockerby DA, Borg MK, Nicholls WD, Reese JM. Molecular dynamics pre-simulations for nanoscale computational fluid dynamics. *Microfluid Nanofluidics* 2015;18:461–74.
- [92] Whitaker S. Flow in porous media I: a theoretical derivation of Darcy's law. *Transport Porous Media* 1986;1(1):3–25.